Dalton Transactions

ROYAL SOCIETY OF CHEMISTRY

PAPER

Check for updates

Cite this: *Dalton Trans.*, 2022, **51**, 10909

Spin transitions in ferric catecholate complexes mediated by outer-sphere counteranions†

Maxim Chegerev,*[a] Oleg Demidov,[b] Pavel Vasilyev,[c] Nikolay Efimov,[c] Stanislav Kubrin,[d] Andrey Starikov,[a] Valery Vlasenko,[d] Alexander Piskunov,[e] Svetlana Shapovalova,[f] Alexander Guda,[f] Yury Rusalev[f] and Alexander Soldatov[f]

Received 18th April 2022,
Accepted 27th June 2022

DOI: 10.1039/d2dt01207c

rsc.li/dalton

A family of ionic ferric catecholate complexes **1–4** bearing a disubstituted 3,6-di-*tert*-butyl-catecholate ligand (3,6-DBCatH_2) and tetradentate tris(2-pyridylmethyl)amine (TPA) was prepared and its spin transitions were investigated. Variation of the outer-sphere counteranions (PF_6, BPh_4, ClO_4, BF_4) is accompanied by changes in the magnetic behavior of the compounds under consideration. The crystal structures of complexes **1**, **3** and **4** were determined by single crystal X-ray diffraction analysis at 100 K and 293 K. The complexes were characterized by the occurrence of a thermally induced spin-crossover process in the solid state with different degrees of completeness, which was confirmed by the comprehensive spectroscopic investigation (EPR, magnetic susceptibility, Mössbauer, and XAS) of the isolated compounds. Complex **4** containing BF_4 anions was found to demonstrate valence tautomeric transition along with spin-crossover. This finding makes compound **4** the first salt-like mononuclear ferric catecholate complex exhibiting valence tautomerism.

Introduction

Metal complexes with redox-active ligands are attracting considerable attention from scientists in the last 40 years.[1–5] It is caused by the unique ability of such types of ligands, being coordinated to the metal center, to change their oxidation state reversibly. Redox-active ligands can be used as reservoirs of electrons, for designing highly-active catalysts for bond-forming or bond-breaking chemical reactions,[6–10] for generating ligand-centered radicals applied in the directed preparation of polyspin systems—building blocks of molecular magnets.[11–15]

Among the variety of magnetically active compounds, a fairly commonly used structural motif is 3d-metal ionic complexes consisting of one redox-active ligand (usually dioxolene) and a tetradentate nitrogen-containing base (tris(2-pyridylmethyl)amine (TPA), *N*,*N*′-dialkyl-2,11-diaza[3.3]-(2,6)pyridinophanes and others).[16,17]

Increased attention to the ferric catecholate (Cat) systems is caused by their capability to act as promising functional models of intra- and extradiol catechol dioxygenases.[18–23] Presently, a number of Fe^{III} complexes chelated by tetradentate N-donor bases and various functionalized Cat-ligands have been prepared and their catalytic ability in oxygenative aromatic C–C bond cleavage reactions has been studied. It was established that the presence of electron-donating substituents in the Cat moiety increases the accessibility of the Fe^{II}-SQ (SQ—radical-anionic semiquinonate form of dioxolene) state responsible for the reaction of ferric catecholate complexes with dioxygen.[22,24]

On the other hand, such types of complexes were found to exhibit magnetic bistability caused by the spin-crossover (SCO) phenomenon, consisting of reversible changes in the spin state of the metal ion.[25,26] A number of papers on iron(III) catecholate complexes with the general formulae $[(TPA)Fe(R\text{-}Cat)]^+$ bearing substituted catecholates (R = H, alkyl, alkoxy, Cl, NO_2) were published.[27–30] The molecular and electronic structures of these compounds were analyzed by a variety of spectroscopic and computational methods. It was revealed that the electronic properties of the substituents in the Cat-ligand have

[a]*Institute of Physical and Organic Chemistry, Southern Federal University, Stachki Avenue, 194/2, 344090 Rostov-on-Don, Russia. E-mail: mchegerev@sfedu.ru*
[b]*North Caucasus Federal University, Pushkin st. 1, 355017 Stavropol, Russia*
[c]*Kurnakov Institute of General and Inorganic Chemistry, Leninsky avenue, 31, 119991 Moscow, Russia*
[d]*Institute of Physics, Southern Federal University, Stachki Ave., 194, 344090 Rostov-on-Don, Russia*
[e]*Razuvaev Institute of Organometallic Chemistry, Russian Academy of Sciences, 49 Tropinina Str., GSP-445, 603950 Nizhny Novgorod, Russia*
[f]*The Smart Materials Research Institute, Southern Federal University, Sladkova 178/24, 344090 Rostov-on-Don, Russia*

† Electronic supplementary information (ESI) available: Crystallography data, FT-IR, UV-vis, Mössbauer spectra, DFT calculations. CCDC 2164133, 2164135, 2164127, 2164128, 2164132 and 2164130. For ESI and crystallographic data in CIF or other electronic format see DOI: https://doi.org/10.1039/d2dt01207c

This journal is © The Royal Society of Chemistry 2022

a significant influence on the SCO equilibrium between the low-spin (S = 1/2) and high-spin (S = 5/2) states. Moreover, a detailed computational density functional theory (DFT) study points to a significant quantum mixing of close by energy Fe^{III}-Cat and Fe^{II}-SQ electronic configurations, and the insertion of electron-donating groups into the Cat moiety increases the contribution of the Fe^{II}-SQ state. An electron paramagnetic resonance (EPR) investigation of the electronic structure of such types of ferric complexes in the low-spin state confirmed this assumption. The anisotropy of the g-tensor is markedly reduced when the dioxolene varies from 4,5-di-nitro-catecholate to 3,5-di-*tert*-butyl-catecholate (3,5-DTBCat), which corresponds to the increase in the Fe^{II}-SQ character in the mixture with the Fe^{III}-Cat configuration.[31]

Recently, a comprehensive investigation of the SCO iron(III) catecholate complex $[(TPA)Fe^{III}(CAT\text{-}NN)]BPh_4$ functionalized with a stable nitronylnitroxide radical (NN) was described.[32] Upon excitation of the ligand-to-metal charge transfer band (LMCT), a short-lived Fe^{II}-SQ state is populated, which rapidly relaxes into a metastable ls-Fe^{III}Cat (ls = low-spin) state followed by the repopulation of the hs-Fe^{III}Cat (hs = high-spin) ground state. It was found that insertion of the NN-radical in the catecholate ring increases the multiplicity of the system, but has a negligible effect on the SCO and photophysical processes.

Another promising feature of ionic metal complexes with catecholate ligands is their capability to exhibit the redox-isomerism (or valence tautomerism (VT)) phenomenon. This process is well known for cobalt systems and involves a reversible intramolecular electron transfer between the metal center and a redox-active ligand (ls-Co^{III}-Cat ⇄ hs-Co^{II}-SQ) induced by variation of external stimuli (temperature, pressure or light irradiation).[33,34] At the same time, despite numerous discussions, the VT phenomenon has not yet been observed in ionic ferric catecholate compounds.

Additionally, there are some studies regarding N_4–Fe dioxolene complexes with other than Fe^{III}-Cat charge distribution. The unusual hs-Fe^{II}-Cat species bearing the methylated Me_3TPA ligand and 3,5-DTBCatH monoanion were found to be catalytically active in extradiol-cleaving reactions.[35,36] Rare examples of dicationic ls-Fe^{III}-SQ complexes consisting of 3,5-DTBSQ[37] and imSQ[38] (where 3,5-DTBSQ = 3,5-di-*tert*-butyl-semiquinonate and imSQ = 4,6-di-*tert*-butyl-2-iminosemiquinonate) have been prepared and studied. It was shown that the compounds are diamagnetic (S = 0) due to the strong antiferromagnetic coupling of the low-spin Fe^{III} (S = 1/2) and SQ-radical (S = 1/2) paramagnetic centres, which makes them inactive towards the catechol cleavage reactions. Nevertheless, a recent DFT theoretical investigation[39] has revealed the possibility of thermally initiated SCO in such types of compounds.

In this paper, we report a comprehensive study of the ionic ferric complexes **1–4** [(TPA)Fe(3,6-DBCat)]X (where X = PF_6, BPh_4, ClO_4, and BF_4) based on the symmetrically substituted 3,6-di-*tert*-butyl-catechol ligand (Scheme 1). The spin interconversions were investigated through variable-temperature single-crystal X-ray diffraction, DFT calculations, and magnetic, Mössbauer and X-ray absorption spectroscopy (XAS) measurements. It should be noted that complex **2** containing the BPh_4 anion was earlier prepared in ref. 22 and studied in terms of its catalytic activity as catechol-dioxygenase, while its magnetic properties were not investigated.

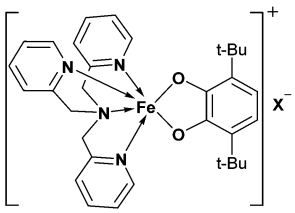

X = PF_6(**1**); BPh_4(**2**); ClO_4(**3**); BF_4(**4**)

Scheme 1 Ferric complexes under investigation.

Experimental

Materials and methods

All manipulations were carried out under vacuum using standard Schlenk techniques. The solvents were purified using standard methods. The reagents $FeCl_3$, $Fe(ClO_4)_3{\cdot}6H_2O$, $NaBF_4$, $NaBPh_4$, and KPF_6 were purchased from Alfa-Aesar and used without any additional purification. The TPA ligand[40] and 3,6-di-*tert*-butyl-catechol[41] were synthesized according to the reported procedures. EPR measurements were carried out using an X-band spectrometer Bruker EMX Plus. The theoretical spectrum was calculated using the Bruker WinEPR Simfonia v.1.25 program. High-resolution mass spectra were recorded using a Bruker maXis Impact UHR-TOF mass spectrometer (electrospray ionization). The elemental analysis was performed using an Elementar Vario EL cube elemental analyzer.

Magnetic measurements

Magnetic susceptibility measurements were performed using a Quantum Design PPMS-9 susceptometer in the temperature range of 2–300 K at an applied magnetic field of 5 kOe. The measurements were carried out using polycrystalline samples covered with mineral oil and sealed in a polyethylene bag in order to prevent field-induced torquing of the crystals. The magnetic data were corrected for the contributions from the sample holder and mineral oil and the intrinsic diamagnetism estimated from Pascal's constants.

Mössbauer measurements

Mössbauer spectra were recorded using an MS1104Em spectrometer. The ^{57}Co in the Rh matrix was used as a source of gamma radiation. During cooling, the samples were placed into the camera of a CCS-850 helium cryostat. The isomer shifts δ are given relative to α-Fe.

Crystallography

The X-ray diffraction datasets were recorded using an Agilent SuperNova diffractometer using a microfocus X-ray radiation

 This journal is © The Royal Society of Chemistry 2022

source with copper anode and Atlas S2 two-dimensional CCD detector. The reflections were recorded and the unit cell parameters were determined and refined using the dedicated CrysAlisPro 171.41.93a software suite.[42] The structure was solved with the ShelXT program[43] and refined with the ShelXL program.[44]

XAS measurements

In situ X-ray absorption spectroscopy study was performed at the beamline "Structural Materials Science"[45] using the equipment of Kurchatov Synchrotron Radiation Source (Moscow, Russia). The storage ring with an electron beam energy of 2.5 GeV and a current of 40–80 mA was used as the source of radiation. All the spectra were collected in the transmission mode using a Si(111) channel-cut monochromator. Three ionization chambers were used to monitor the intensity of the X-ray beam and measure the spectra of the sample simultaneously with Eu_2O_3 as the reference for energy calibration. The sample pellet was placed in an SRDK-408D2 cryocooler of Sumitomo Heavy Industries to cool down to the liquid helium temperature.

IR and UV-vis measurements

The infrared spectra were recorded using a Vertex 70 (Bruker, Billerica, MA, USA) spectrometer equipped with a MCT (mercury–cadmium–telluride) detector. A Praying Mantis low-temperature reaction chamber (Harrick Scientific Products Inc., New York, USA) installed in the spectrometer was used to record the diffuse reflectance infrared Fourier-transform (DRIFT) spectra at variable temperatures. All measurements were performed under a nitrogen atmosphere inside the reaction chamber at temperatures ranging from 300 K down to 123 K using a powdered sample thoroughly milled in a mortar. All spectra were recorded with a 1 cm^{-1} energy resolution for 64 scans and transformed into absorption spectra using the Kubelka–Munk function.

The UV-vis spectra were recorded in acetone using a dual-beam optical spectrophotometer UV-2600 (Shimadzu) with a single monochromator. The measurements were carried out in the transmittance mode within 300–900 nm at a step of 2 nm with subsequent conversion to absorption.

Computational details

The density functional theory calculations were performed using the Gaussian 16 program package[46] with the UTPSSh functional[47] and the 6-311++G(d,p) basis set including the diffuse and polarization functions of all atoms. The stationary points of the potential energy surfaces (PESs) were located by full geometry optimization with the calculation of force constant matrices indicating the correspondence of the structures obtained to the minima on the PES and checked for the stabilities of DFT wave function.

Synthetic procedures

Complex 1 Anhydrous $FeCl_3$ (0.084 g, 0.52 mmol) was placed in an ampoule and dissolved in 5 ml of methanol. To this ampoule, a solution of TPA (0.15 g, 0.52 mmol) in the same solvent (10 ml) was added and the reaction mixture was stirred at 70 °C for 30 min. After this it was treated with a solution containing 3,6-DBCatH_2 (0.115 g, 0.52 mmol) and triethylamine (0.15 mL, 1.0 mmol) in methanol (10 mL). An immediate color change from orange-yellow to intense blue occurred. The reaction mixture was stirred for another 1 h and a (1 : 1) water–methanolic solution of KPF_6 (0.15 g, 0.80 mmol) was added. The ampoule was placed in a refrigerator (−4 °C) and kept undisturbed for 1 day. Dark-blue needle-like crystals of complex **1** were isolated by vacuum filtration, washed with methanol and dried under vacuum. Yield 0.303 g (82%).

Complexes 2 and **4** were prepared according to the procedure described above with $NaBPh_4$ (0.27 g, 0.80 mmol) and $NaBF_4$ (0.09 g, 0.80 mmol) as the sources of desired counterions. Yields: 0.368 g (80%) for **2** and 0.264 g (78%) for **4**.

Complex 3 was prepared using $Fe(ClO_4)_3{\cdot}6H_2O$ salt as a starting material. $Fe(ClO_4)_3{\cdot}6H_2O$ (0.24 g (0.52 mmol) was placed in an ampoule and dissolved in 5 ml of methanol. To this ampoule, a solution of TPA (0.15 g, 0.52 mmol) in the same solvent (10 ml) was added and the reaction mixture was stirred at 70 °C for 30 min. After this it was treated with a solution containing 3,6-DBCatH_2 (0.115 g, 0.52 mmol) and triethylamine (0.15 mL, 1.0 mmol) in methanol (10 mL). An immediate color change from light-yellow to intense blue occurred. The reaction mixture was stirred for 15 min, placed in a refrigerator (−4 °C) and kept undisturbed for 1 day. Dark-blue block-shaped crystals of complex **3** were isolated by vacuum filtration, washed with methanol and dried under vacuum. Yield 0.294 g (85%).

1: Anal. Calcd for $C_{32}H_{38}F_6FeN_4O_2P{\cdot}(H_2O)_{0.5}$: C, 53.42; H, 5.46; N, 7.76. Found: C, 53.32; H, 5.56; N, 7.70.

ESI-MS (*m*/*z*): 566.23 $[M]^+$.

UV-vis (acetone) λ_{max}, nm (ε): 593 (1675), 893 (2210).

2: Anal. Calcd for $C_{56}H_{58}BFeN_4O_2$: C, 75.94; H, 6.60; N, 6.33. Found: C, 75.84; H, 6.71; N, 6.24.

ESI-MS (*m*/*z*): 566.23 $[M]^+$.

UV-vis (acetone) λ_{max}, nm (ε): 580 (1710), 881 (2190).

3: Anal. Calcd for $C_{32}H_{38}ClFeN_4O_6{\cdot}(H_2O)_{0.5}$: C, 57.03; H, 5.83; N, 8.31. Found: C, 57.14; H, 5.92; N, 8.25.

ESI-MS (*m*/*z*): 566.23 $[M]^+$.

UV-vis (acetone) λ_{max}, nm (ε): 590 (1680), 897 (2230).

4: Anal. Calcd for $C_{32}H_{38}BF_4FeN_4O_2{\cdot}(H_2O)_{0.5}$: C, 58.12; H, 5.94; N, 8.47. Found: C, 58.22; H, 6.02; N, 8.37.

ESI-MS (*m*/*z*): 566.23 $[M]^+$.

UV-vis (acetone) λ_{max}, nm (ε): 587 (1667), 892 (2160).

Results and discussion

Crystal structures

Compounds **1–4** under study were prepared through the reactions commonly used for the synthesis of the (TPA)Fe^{III}(Cat) complexes.[27–29] At the first stage, ferric chloride reacted with the TPA ligand in a methanol solution. Further reaction with deprotonated 3,6-DBCatH_2 is accompanied by a colour change

from yellow to dark blue-violet. Metathesis reactions with the corresponding KPF_6, $NaBPh_4$, and $NaBF_4$ salts result in the precipitation of the desired compounds **1**, **2**, and **4** as dark-blue crystals. In the case of complex **3**, ferric perchlorate salt was used as the starting material (Scheme 1).

Single crystals of complexes **1**, **3** and **4** suitable for X-ray diffraction analysis were obtained after storing the reaction mixtures in a refrigerator at −4 °C for 1 day. Compounds **1**, **3** and **4** were found to contain half of solvate H_2O molecules per complex in the crystal cell. The molecular structures of **1**, **3** and **4** were determined at two temperatures (T_1 = 293 K and T_2 = 100 K). In all the cases, a slight disorder of counterions was observed, and additionally, in **3** and **4** the pyridine moieties of TPA are disordered. Compound **1** crystallizes in the orthorhombic space group *Pbcn* (Z = 8, Z' = 1), while **3** and **4** are described by the $P\bar{1}$ triclinic space groups (Z = 2, Z' = 1) with close unit cell parameters. Selected bond lengths and angles are listed in Table 1. The crystal structure of complex **2** was determined earlier[22] at 223 K only.

According to the X-ray diffraction data, the metal centre in all six-coordinate iron complexes **1**, **3** and **4** possesses a distorted octahedral geometry composed of four nitrogen atoms of the tetradentate TPA ligand, and two oxygen atoms of the catecholate ligand (**1**, Fig. 1). The structure of the obtained compounds contains one outer-sphere anion (PF_6, ClO_4, and BF_4) and the 1+ charged [(TPA)Fe(3,6-DBCat)] core. Analysis of the crystal packing of complexes under study revealed the presence of weak intermolecular interactions of various nature: H_2O···anion, CH···anion, H_2O···HC, and, additionally, π–π stacking interactions (~3.6 Å) between pyridine moieties of adjacent TPA ligands (see ESI, Fig. S1 and S2†).

Analysis of metrical parameters collected at 293 K clearly indicates the inclusion of the metal centre in compounds **1**, **3** and **4** in the high-spin state (Table 1). The average interatomic

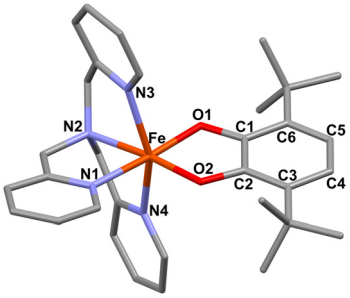

Fig. 1 X-ray structure of the cationic part of **1** at 293 K. The PF_6 anion and H-atoms are omitted for clarity.

distances for **1** (Fe–O = 1.907 Å and Fe–N = 2.161 Å), **3** (Fe–O = 1.902 Å and Fe–N = 2.161 Å), and **4** (Fe–O = 1.898 Å and Fe–N = 2.165 Å) are characteristic for previously described hs-ferric catecholate compounds.[28,29] Analysis of the N3–Fe–N4 angles between the metal ion and the two opposite N donor atoms of TPA (153° for **1**, 156° for **3**, and 151° for **4**) reflects the significant distortion of the coordination polyhedron from the ideal octahedron (180°).

It is interesting to note that the coordination of 3,6-di-*tert*-butyl-catecholate dianions to metal centres in all compounds under consideration was found to be slightly asymmetric. The differences in Fe–O1 and Fe–O2 bonds amount to 0.009 Å for complex **1**, 0.027 Å for **3**, and 0.035 Å for **4**.

In complex **1** the C–O (~1.34 Å) and ring C–C (~1.40 Å) bond lengths in the catecholate moiety indicate the dianionic nature of the redox-active ligand.[48] In 2012, Brown proposed to use the "metrical oxidation state" (MOS) approach to determine the redox state of the dioxolene ligands.[49] According to this, the catecholate MOS index is −2; for semiquinonate, it is −1 and it is 0 for quinone ligand. The calculated MOS for

Table 1 Selected bond lengths (Å) and bond angles (°) of complexes **1**, **3** and **4**

	1		**3**		**4**	
T/K	293	100	293	100	293	100
Fe–O1	1.912(1)	1.916(1)	1.916(1)	1.902(1)	1.916(2)	1.898(2)
Fe–O2	1.903(1)	1.903(1)	1.889(2)	1.854(1)	1.881(2)	1.857(2)
Fe–N1	2.130(2)	2.113(1)	2.151(2)	1.965(1)	2.151(3)	1.966(2)
Fe–N2	2.201(2)	2.186(2)	2.171(2)	1.995(2)	2.175(3)	2.001(2)
Fe–N3	2.163(2)	2.133(1)	2.170[a]	1.970(2)	2.160(3)	1.979(3)
Fe–N4	2.151(2)	2.145(1)	2.154(2)	1.961(2)	2.173[a]	1.966(3)
C1–O1	1.340(2)	1.343(2)	1.342(2)	1.336(2)	1.338(3)	1.337(3)
C2–O2	1.347(2)	1.351(2)	1.348(2)	1.342(2)	1.356(3)	1.337(3)
C1–C2	1.428(3)	1.424(2)	1.423(3)	1.425(2)	1.423(4)	1.425(4)
C1–C6	1.399(3)	1.407(2)	1.401(2)	1.416(2)	1.412(4)	1.415(3)
C2–C3	1.400(3)	1.406(2)	1.398(3)	1.413(2)	1.395(4)	1.409(4)
C3–C4	1.394(3)	1.397(2)	1.377(3)	1.386(2)	1.390(5)	1.385(4)
C4–C5	1.388(4)	1.394(3)	1.389(4)	1.401(3)	1.389(6)	1.400(4)
C5–C6	1.391(3)	1.393(2)	1.389(3)	1.390(3)	1.383(5)	1.388(4)
O1–Fe–O2	84.59(6)	84.79(5)	84.80(6)	85.84(5)	84.88(1)	85.94(8)
N2–Fe–N1	80.52(6)	80.97(5)	80.34(7)	85.59(6)	80.08(1)	85.64(9)
N3–Fe–N4	153.05(7)	154.21(6)	155.9(2)	165.57(6)	151.11[a]	165.4(1)
N1–Fe–O2	96.16(6)	94.88(5)	93.94(7)	94.38(6)	93.48(1)	94.19(9)
N2–Fe–O1	99.00(6)	99.57(5)	100.93(6)	94.20(6)	101.56(1)	94.24(9)

[a] Average value was taken due to a slight disorder in TPA.

 This journal is © The Royal Society of Chemistry 2022

complex **1** is −1.80, which allows us to refer it as catecholate. The same situation was found in the cases of complexes **3** and **4**, where the MOS parameters are slightly lower and amount to −1.77 and −1.70 respectively. Nevertheless, it should be noted, that the deviation of the calculated MOS parameters from −2 points to the small "semiquinone-like" alteration of catecholate bonds. Such distortions were discussed previously in[28,29] and explained as a quantum mixing of possible Fe^{III}-Cat and Fe^{II}-SQ electronic configurations.

Significant changes in the metal–donor atom bond lengths of the FeN_4O_2 cores (Table 1) were found in the X-ray diffraction data of complexes **3** and **4** collected at 100 K, which can be attributed to the hs-to-ls conversion. Spin transitions are accompanied by shortening the characteristic interatomic distances by about 0.189 Å (Fe–N) and 0.023 Å (Fe–O) in complex **3**, and 0.185 Å (Fe–N), and 0.020 Å (Fe–O) for complex **4**. The average <Fe–N> = 1.97 Å and <Fe–O> = 1.83 Å bond lengths for the compounds **3** and **4** are comparable with the described low-spin ferric catecholates,[28,29] and it allows one to assign them as ls-Fe^{III} states. Remarkably, the characteristic N3–Fe–N4 angles also changed upon lowering the temperature (165° for **3**, and 166° for **4**) leading to a less distorted octahedron in comparison with the structural data at 293 K (about 10°).

The calculated MOS indexes at low temperature in the case of **3** (−1.64) and **4** (−1.63) point to the catecholate nature of the redox active ligand, but in comparison with MOS at 293 K, the alternation of C–C bonds is slightly larger, which reflects the stronger quantum mixing of the Cat-Fe^{III} and SQ-Fe^{II} configurations.[29] Thus, the metrical data obtained clearly indicates the temperature induced spin-crossover ($S = 5/2 \rightarrow S = 1/2$) transition in compounds **3** and **4**.

In contrast to the mentioned above, lowering the temperature does not significantly change the Fe–N and Fe–O interatomic distances in complex **1**. The average Fe–N = 2.144 Å bond length is slightly shorter than that obtained at 293 K (2.161 Å) but longer than that discussed previously for **3** and **4**. The Fe–O bonds remain practically unchanged. Such relatively small bond contraction (only 0.017 Å) can be explained by the appearance of the ls-fraction, having shorter metal–donor atom bonds, due to the incomplete spin-crossover in **1**. This assumption is in good agreement with magnetic and Mössbauer data, demonstrating the 92% hs to 8% ls ratio at 100 K (see below).

Structural data published[22] on complex **2** (collected at 223 K) was found to be intermediate between the ls-Fe^{III} and hs-Fe^{III} states. The average Fe–O (1.891 Å) and Fe–N (2.056 Å) bond lengths are shorter than those in the pure hs-state but longer than those characteristic for the ls-Fe^{III} catecholate complexes[29] and **3**, **4**. These deviations are in accordance with the Mössbauer data, which indicate the presence of the ls fraction (about 25%) at 225 K (see below).

UV-vis measurements

For synthesized complexes **1–4**, the UV-vis spectra were recorded in acetone at room temperature. All solutions are characterized by intense dark-blue coloration. As reported for many catecholato iron(III) complexes having an octahedral geometry, **1–4** exhibit typical two intense absorption maxima in the visible (~580 nm) and near-IR (~890) regions assigned for Cat → Fe LMCT transitions.[22,28,32] The spectrum of complex **4** is presented in Fig. S3.†

EPR of low-spin isomers of 3 and 4

With the aim to shed light on the electronic structure of low-spin ($S = 1/2$) isomers of compounds **3** and **4**, X-band EPR measurements were performed. Previously a considerable dependence of the anisotropy of the *g*-tensor of unpaired electrons on the electronic properties of the coordinated catecholate ligand in [(TPA)Fe(R-Cat)]X systems was described.[31] Using the more electron-withdrawing 3,4-dinitro-substituted Cat ligand leads to an increase in anisotropy, while in the case of donating 3,5-di-*tert*-butyl-catecholate, the anisotropy of *g*-tensor is reduced. As we discussed above, this finding can be described by the strong quantum mixing of the possible Fe^{III}-Cat and Fe^{II}-SQ electronic configurations. The electron-donating ability of the redox-active ligand directly affects the degree of delocalization of the unpaired electron over the metallacycle, and therefore, the contribution of the two discussed states.

The corresponding spectra of ls isomers of **3** and **4** were registered in frozen CH_2Cl_2 solutions at 100 K. During the cooling of the samples, the colour gradually changed from dark blue to dark green. The obtained EPR spectrum of compound **4** is presented in Fig. 2. Complex **3** is characterized by a similar spectrum (see Fig. S4†), and here only the spectrum of **4** is discussed.

The ls ($S = 1/2$) signal is shown to be pseudo-axial with $g_\perp > g_\parallel$. Analysis of the data obtained allowed us to extract experimental *g* parameters: $g_\perp = 2.116$ and $g_\parallel = 1.980$. Anisotropy was

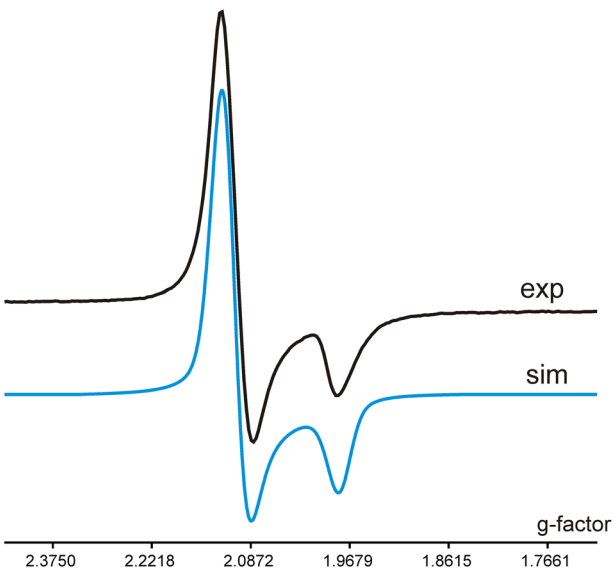

Fig. 2 EPR spectrum of the low-spin isomer of **4** in frozen CH_2Cl_2 solution at 100 K.

estimated as ($g_\perp - g_\parallel$) and amounts to 0.136. It should be noted that in comparison with the previously published EPR data on ferric catecholate systems,[31] our complexes on the basis of 3,6-di-*tert*-butyl-substituted catechol were found to demonstrate reduced anisotropy. For example, evaluated anisotropy in the close by structure 3,5-di-*tert*-butyl-catechol complex was found to be 0.233. According to the data obtained we can conclude that in our case compound **4** is characterized by the increased contribution of the Fe^{II}-SQ state.

Magnetic susceptibility measurements

Magnetic susceptibility plots of **1–4** are shown in Fig. 3. In Table 2 the $\chi_M T$ values observed at the high and low temperatures are gathered. The $\chi_M T$ of compound **1** shows an almost constant value of 4.42 cm^3 K mol^{-1} in the temperature range of 300–200 K, which corresponds to 100% of the hs-Fe^{III} (S = 5/2) configuration.[28,29] Further decreasing the temperature to 30 K leads to the minor lowering of the $\chi_M T$ value to 4.21 cm^3 K mol^{-1}, which can be explained by the presence of an ls-Fe^{III} fraction at this temperature due to the incomplete spin-crossover (~11% according to Mössbauer data). It is in good agreement with the X-ray diffraction data demonstrating insignificant changes in coordination bond lengths upon cooling. The

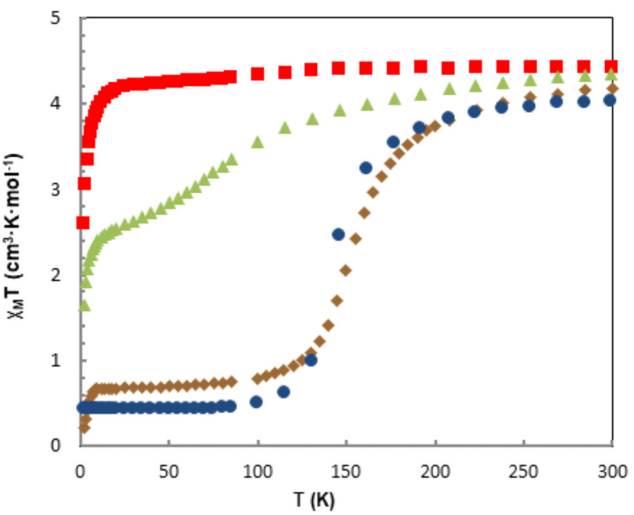

Fig. 3 Temperature dependence of the $\chi_M T$ values of the solid samples of **1** (■), **2** (▲), **3** (●), and **4** (◆).

Table 2 Experimental $\chi_M T$ values measured at low and high temperatures

Compound	T (K)	$\chi_M T$ (cm^3 K mol^{-1})
1	300	4.42
	50	4.25
2	300	4.34
	50	2.84
3	300	4.03
	50	0.43
4	300	4.20
	50	0.69

$\chi_M T$ value of complex **2** at 300 K amounts to 4.34 cm^3 K mol^{-1}, which is close to that found for **1** and points to a pure high-spin (S = 5/2) Fe^{III} state. At lower temperatures, the $\chi_M T$ value shows a gradual decrease and reaches the value of 2.62 cm^3 K mol^{-1} at 30 K. In this case, incomplete spin transition (S = 5/2 → S = 1/2) takes place and the hs:ls ratio can be estimated as 50 : 50. The detailed analysis of the Mössbauer data confirms this estimation, indicating the presence of 55% of low-spin state in the mixture with 45% of hs-Fe^{III} at a given temperature (see below).

More substantial changes in magnetic susceptibility were observed in the cases of compounds **3** and **4**. Similar to the abovementioned data, the high temperature $\chi_M T$ values amount to 4.03 cm^3 K mol^{-1} and 4.20 cm^3 K mol^{-1}, respectively, which are close to that expected for the hs-state. The $\chi_M T$ value of compound **3** shows an insignificant lowering of the temperature in the range of 300–170 K, but further cooling is accompanied by a sharp decrease and the value of $\chi_M T$ at 100 K equals to 0.45 cm^3 K mol^{-1}. This value is characteristic of low-spin catecholate ferric systems with S = 1/2.[28,29] The $T_{1/2}$, defined as the temperature at which the hs and ls fractions are the same, is 150 K. Thus, the magnetic susceptibility of **3** reflects the change in the spin state from the low-spin iron(III) at lower temperatures to high-spin iron(III) at higher temperatures. An analogous behaviour was observed in complex **4**. The $\chi_M T$ value of **4** shows an almost unchanged value of 4.03 cm^3 K mol^{-1} in the temperature range of 300–200 K. At lower temperatures, the $\chi_M T$ value demonstrates a sharp decrease to reach a plateau (at 100 K) with a value close to 0.69 cm^3 K mol^{-1}, characteristic of the ls-Fe^{III} (S = 1/2) configuration. A slight deviation of the obtained result from complex **3** and the literature analogues[28,29] can be explained by the presence of about 13% of molecules trapped in the hs-state at 14 K, according to the Mössbauer data. The estimated $T_{1/2}$ is equal to 155 K.

It should be noted that the analysis of magnetic susceptibility data does not allow ones to unequivocally distinguish two possible Cat-Fe^{III} and SQ-Fe^{II} electronic configurations, which are characterized by the same multiplicity. In the first case, all five unpaired electrons are localized on the ferric centre S_{Fe} = 5/2, while the second system can be described as 4/2 + 1/2 (from hs-Fe^{II} and SQ-radical). According to the literature, the exchange interactions between the two paramagnetic centres bear a ferromagnetic character, leading to the total S = 5/2 state.[17] Nevertheless, this situation can be clearly solved by performing Mössbauer measurements, which are very sensitive towards the spin and oxidation states of the iron centre.

Mössbauer measurements

Variable temperature ^{57}Fe Mössbauer spectra were recorded for complexes **1–4**. The least square fitting parameters are provided in Table 3. The Mössbauer spectra of compound **4** are shown in Fig. 4. The spectra of **1**, **2** and **3** can be found in the ESI (Fig. S5–S7†).

In the case of complex **1**, the spectrum at 300 K exhibits a well-resolved quadrupole doublet (D1), with a value of the isomer shifting (IS) δ = 0.40 mms^{-1} and the quadrupole split-

 This journal is © The Royal Society of Chemistry 2022

Table 3 Selected ^{57}Fe Mössbauer fitted parameters of compounds **1–4**

T (K)	Component	$\delta \pm 0.02$ (mm s^{-1})	$\Delta E_Q \pm 0.02$ (mm s^{-1})	$A \pm 1$ (%)	Fe state
	Complex 1				
300	D1	0.40	1.42	100	hs-Fe^{III}
160	D1	0.50	1.47	96	hs-Fe^{III}
	D2	0.23	1.86	4	ls-Fe^{III}
14	D1	0.52	1.54	87	hs-Fe^{III}
	D2	0.25	1.94	13	ls-Fe^{III}
	Complex 2				
300	D1	0.40	1.30	100	hs-Fe^{III}
160	D1	0.41	1.55	61	hs-Fe^{III}
	D2	0.26	1.76	39	ls-Fe^{III}
14	D1	0.44	1.54	45	hs-Fe^{III}
	D2	0.27	1.82	55	ls-Fe^{III}
	Complex 3				
300	D1	0.42	1.44	100	hs-Fe^{III}
160	D1	0.42	1.42	42	hs-Fe^{III}
	D2	0.26	1.63	59	ls-Fe^{III}
14	D1	0.42	1.34	6	hs-Fe^{III}
	D2	0.28	1.66	94	ls-Fe^{III}
	Complex 4				
300	D1	0.39	1.32	54	hs-Fe^{III}
	D2	0.85	0.81	46	hs-Fe^{II}
160	D1	0.42	1.45	66	hs-Fe^{III}
	D2	0.78	0.68	12	hs-Fe^{II}
	D3	0.26	1.64	22	ls-Fe^{III}
14	D1	0.42	1.36	9	hs-Fe^{III}
	D2	0.75	0.69	4	hs-Fe^{II}
	D3	0.27	1.67	87	ls-Fe^{III}

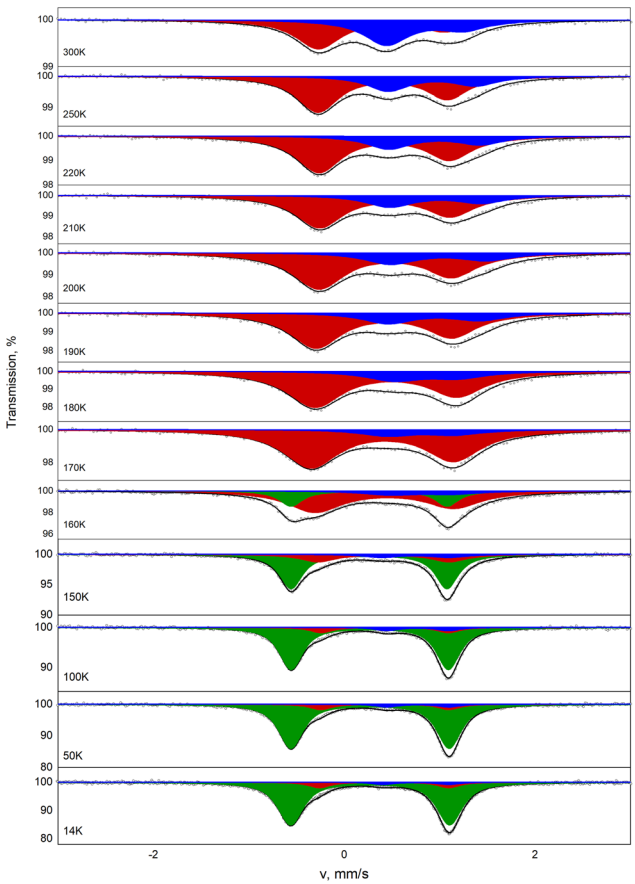

Fig. 4 Variable temperature ^{57}Fe Mössbauer spectra of **4** (green – ls-Fe^{III}, red – hs-Fe^{III}, and blue – hs-Fe^{II}).

ting (QS) ΔE_Q = 1.42 mms^{-1}. These values are comparable to those given for previous ferric catecholate[28,29] studies and some biological systems[50] and correspond to the hs-Fe^{III} state. It should be noted that in the high-spin Fe^{III} state, different broadening of the lines with decreasing temperature was observed, which can be explained by its slow paramagnetic relaxation. The subsequent lowering of the temperature up to 14 K is accompanied by the appearance of the other quadrupole doublet (D2) (in addition to that observed at 300 K) with δ = 0.25 mms^{-1} and ΔE_Q = 1.95 mms^{-1}, which is characteristic of the ls-Fe^{III} isomer. The ratio of the intensities of the two found signals was estimated as 87% hs-Fe^{III} and 13% of ls-Fe^{III}, indicating the incomplete SCO transition.

Almost similar behaviour was found for compound **2**. At 300 K the spectrum of **2** also shows a single quadrupole doublet with δ = 0.40 mms^{-1} and ΔE_Q = 1.42 mms^{-1} consistent with the hs-Fe^{III} state. At 14 K, the spectra are composed of two quadrupole doublets with δ = 0.41 mms^{-1} abd ΔE_Q = 1.54 mms^{-1} (45% area, A) and δ = 0.27 mms^{-1} and ΔE_Q = 1.80 mms^{-1} (55% area) corresponding to the ferric high- and low-spin states, respectively. The data obtained points to the incomplete SCO in complex **2**.

The spectra of **3** at 14 K exhibit two well-resolved quadrupole doublets. The major species with δ = 0.28 mms^{-1} and ΔE_Q = 1.66 mms^{-1} are comparable with the literature data[28,29] and account for 94% of the ls-Fe^{III} in the sample. A minority species with a 6% relative area has an isomer shift of 0.42 mms^{-1} and ΔE_Q of 1.34 mms^{-1} and was assigned to the hs-Fe^{III} component. The 300 K spectrum is similar to complexes **1** and **2** and can be unambiguously referred to as pure hs-Fe^{III} (δ = 0.42 mms^{-1} and ΔE_Q = 1.44 mms^{-1}). Thus, in the case of compound **3** we can conclude that virtually a complete (94%) spin-crossover transition (S = 1/2 → S = 5/2) takes place, and only 6% of molecules are trapped in the hs-Fe^{III} state at 14 K. The slight asymmetry of the quadrupole doublets, which disappears upon lowering the temperature, may be attributed to the Goldanskii–Karyagin effect.[51] The Mössbauer data are in good agreement with the structural and magnetic measurements presented above.

A remarkable result was obtained after the detailed analysis of the Mössbauer spectra of complex **4** (Fig. 4 and Table 3). At 300 K, the spectrum is characterized by the presence of the two quadrupole doublets. The first one with δ = 0.39 mms^{-1} and ΔE_Q = 1.32 mms^{-1} corresponds to the hs-Fe^{III} configuration, while the second one with δ = 0.85 mms^{-1} and ΔE_Q = 0.81 mms^{-1} is attributed to hs-Fe^{II}.[52] The relative areas of these two signals are estimated as 54 : 46, respectively, which point to the almost equimolar mixture of the discussed states at 300 K. Cooling to 170 K leads to the change in the ratio of the two observable components to 86 : 16. Further lowering of the temperature is accompanied by the appearance of the additional doublet with an IS of 0.26 mms^{-1} and QS of 1.64 mms^{-1}, belonging to the ls-Fe^{III} configuration. In the temperature range of 160–100 K, the almost complete SCO transition of hs-Fe^{III} to ls-Fe^{III} takes place. The low temperature data at 14 K point to the presence of three different signals

corresponding to the ls-Fe^{III}, hs-Fe^{III} and hs-Fe^{II} fractions with 87%, 9% and 4% relative areas, respectively. The analysis of the obtained results allows us to assume that all the changes found in complex **4** can be divided into two elementary steps: (1) almost complete SCO (ls-Fe^{III} to hs-Fe^{III}) in the 15–170 K temperature range; (2) valence tautomeric transition (hs-Fe^{III}-Cat to hs-Fe^{II}-SQ) above 170 K leading to the formation of the ferrous semiquinonate isomer. This finding makes compound **4** the first mononuclear ferric catecholate system demonstrating VT transition alongside SCO. It should be noted that analogous spin transitions were observed recently in dinuclear (Fe–Co) tetraoxolene-bridged complex demonstrating pyroelectricity upon heating.[53]

This assumption is additionally confirmed by IR spectral analysis, which is known to be an effective tool for the investigation of metal dioxolene complexes.[54,55] It can provide information on the ligand-related processes in the system as each oxidation state of the ligand displays a characteristic pattern of peaks. For instance, coordinated semiquinonate and catecholate ligands display vibrations of C–O bonds in the ranges of 1500–1400 and 1300–1250 cm^{-1}, respectively. Analysis of the experimental data obtained for the solid sample of compound **4** (Fig. S8†) revealed the intense vibrations at 1290 cm^{-1} and 1488 cm^{-1}, which points to the presence of the Cat and SQ states of the dioxolene ligand in **4**. Decreasing the temperature to 123 K is accompanied by the minor changes in the intensities of these two bands, which most likely can be attributed to VT dynamics.

DFT calculations

With the aim to get deeper insights into the electronic structures of the complexes under study, the DFT calculations (UTPSSh/6-311++G(d,p)) were performed. This approximation is known to provide a correct reproduction of the energy and magnetic characteristics of the complexes demonstrating magnetic bistability.[56–59]

The optimized geometries of complexes **1**–**4** in the high-spin and the low-spin states are in good agreement with the experimental data (Fig. S9†). A slight elongation (~5%) of the coordination bond lengths is caused by the fact that the DFT calculations were performed on the isolated molecules, without taking into account the crystal packing forces. The calculated energy gaps between the high- and low-spin isomers of all compounds do not exceed 11 kcal mol^{-1}, which within the framework of this approximation points to the high probability of the thermally initiated SCO.

The analysis of the calculated C–O and C–C bond lengths in the catecholate moieties of $[(TPA)Fe(3,6\text{-}DBCat)]^+$ revealed bond alternation in the hs- and ls-states comparable to the X-ray diffraction data. Thus, the computed values of the interatomic distances are intermediate between the pure catecholate and the *o*-semiquinonate forms of the redox-active ligand.[1,49] This finding is in good agreement with the published data[28,29] and points to the large mixing of the possible Fe^{III}-Cat and Fe^{II}-SQ configurations in both the hs- and ls-states.

According to the DFT calculations, the spin density distributions of all the complexes under consideration are similar,

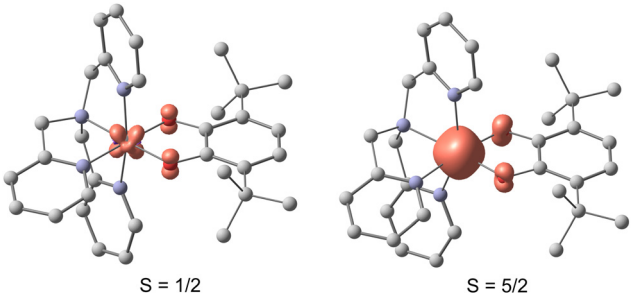

Fig. 5 Spin density distribution (contour value = 0.03 e $Å^{-3}$) in two isomers of complex **4** according to DFT (UTPSSh/6-311++G(d,p)). Hydrogen atoms and counterions are omitted for clarity.

which points to the minor influence of the nature of counteranions on the electronic structures of **1**–**4** (Fig. 5). The calculated q_s^{Fe} values at the high-spin metal centres are equal to 3.82, which is less than the value expected for 5 unpaired electrons. A significant part of the metal spin density is delocalized over the donor atoms ($\sum q_s^{O}$ = 0.56) and C1–C6 of the aromatic ring ($\sum q_S^{ring}$ = 0.33) of the coordinated Cat ligand. The same situation is observed in the low-spin states: the obtained values are q_s^{Fe} = 0.46, $\sum q_s^{O}$ = 0.38 and $\sum q_S^{ring}$ = 0.28. Thus, the calculated q_S^{Fe} values are too high to be assigned to the pure hs-Fe^{II} state and too low to be assigned to the pure hs-Fe^{III} state. This finding confirms the assumption of mixing Fe^{III}-Cat and the close by energy Fe^{II}-SQ configurations.

XAS measurements

In situ temperature dependent Fe K-edge spectra of complex **4** demonstrated reversible changes in the spectral shape upon cooling and heating, indicating the transformation to the ls-Fe^{III} ground state (Fig. 6). The principal component analysis

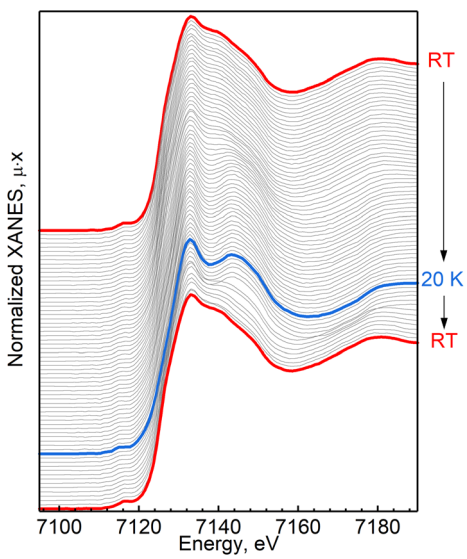

Fig. 6 Temperature-resolved Fe K-edge XANES spectra measured for the solid sample of compound **4** from room temperature (RT) to 20 K and back.

This journal is © The Royal Society of Chemistry 2022

(PCA) of the series of spectra allowed us to distinguish three independent components (Fig. 7a), which were also detected by the Mössbauer spectroscopy measurements. In a second step, we performed the target transformation of the mathematical components and compared the resulting spectra with the literature references. We selected the hs-Fe^{III} and ls-Fe^{III} spectra of the two six-coordinated complexes $Fe(acac)_3$ and $[Fe(HB(pz)_3)_2](ClO_4)$ from Westre[60] and the six-coordinated hs-Fe^{II} complex $[Fe^{II}(5NO_2\text{-salaep})_2]$ from Rakotonandrasana[61] as references (see Fig. S10 and S11† with all the studied references).

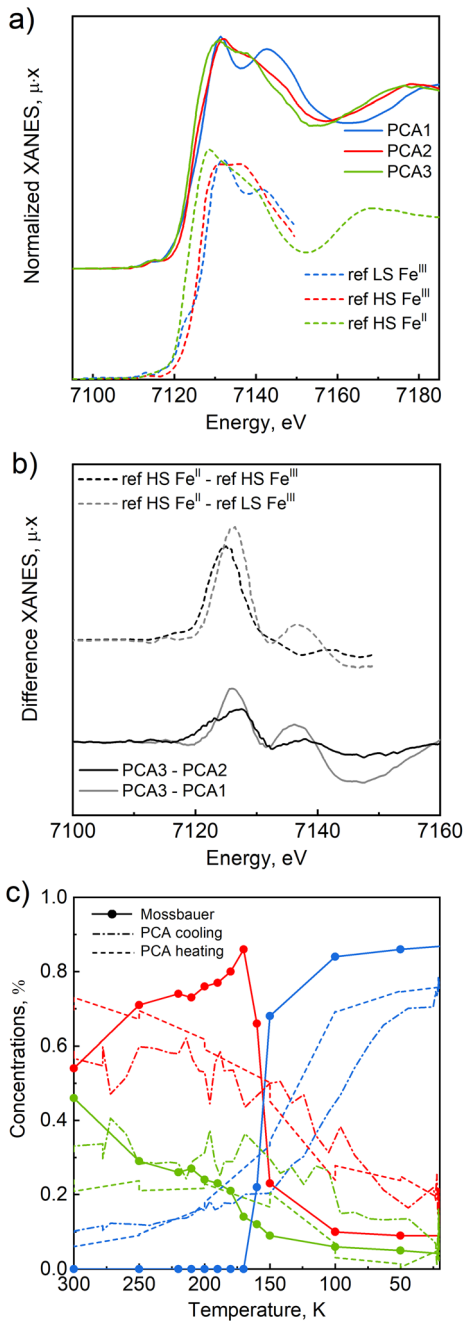

Fig. 7 (a) Three principal components derived from the series of experimental XANES spectra compared to the reference spectra of ls-, hs-Fe^{III} and hs-Fe^{II}; (b) difference in the spectra of the principal components and references; (c) concentrations of the three principal components derived from the series of experimental XAS spectra compared to the concentrations obtained from Mössbauer spectroscopy.

Fig. 7b shows the difference in the XANES spectra calculated for the PCA components and the corresponding references. Such a comparison confirms that the third component PCA3 can be described as in the hs-Fe^{II} state, while the PCA1 and PCA2 components are in the ls-Fe^{III} and hs-Fe^{III}, respectively. The concentrations of the principal components derived from the series of the XANES spectra are in good agreement with the results obtained by the Mössbauer spectroscopy (Fig. 7c). Thus, the X-ray absorption spectroscopy confirms the presence of the SCO + VT changes in complex **4** in the solid state.

Conclusions

The octahedral iron(III) complexes [(TPA)Fe(3,6-DBCat)]X on the basis of the 3,6-di-*tert*-butyl-catecholate ligand and tetradentate TPA with different anions (X = PF_6, BPh_4, ClO_4, and BF_4) have been prepared and characterized. The molecular and electronic structures of the compounds under consideration were investigated through variable-temperature single-crystal X-ray diffraction analysis, DFT calculations, magnetic susceptibility measurements, and EPR, Mössbauer and XAS spectroscopy. All complexes were found to demonstrate magnetic bistability caused by the thermally induced SCO process ($S = 1/2 \rightarrow S = 5/2$) in the solid state with different degrees of completeness, depending on the anion used. Complex **1** with the PF_6 anion exists almost completely in the high-spin Fe^{III} state in all temperature ranges with a small sign of SCO (13% of low-spin Fe^{III}) at 14 K. At the same time, compound **2** with BPh_4 demonstrates a deeper hs-Fe^{III} to ls-Fe^{III} conversion with a practically equimolar ratio of the discussed states at 14 K. In the case of compounds **3** (ClO_4) and **4** (BF_4), a virtually complete (>90%) SCO process takes place. Such an unexpected magnetic behaviour is most likely caused by the differences in the crystal packing of molecules in **1**–**4**. Primarily, compounds **2**,[22] **3** and **4**, in addition to a variety of weak solvent···anion, CH···anion, and solvent···HC interactions, are characterized by the presence of π–π stacking interactions (~3.6 Å) between the pyridine moieties of the adjacent TPA ligands. According to the literature, such types of π–π stacking interactions are known to play an important role in SCO properties.[25,26] At the same time, the π–π stacking is absent in the crystal cell of complex **1**.

The unique result was obtained for complex **4**, which was found to demonstrate the valence tautomeric transition alongside with SCO. At lower temperatures (14–170 K), an almost complete SCO (ls-Fe^{III} to hs-Fe^{III}) takes place, while above 170 K, the VT transition (hs-Fe^{III}-Cat to hs-Fe^{II}-SQ) is revealed, giving rise to the ferrous semiquinonate redox isomer. The formation of the new hs-Fe^{II}-SQ state was unequivocally proved by variable temperature Mössbauer and XAS spectroscopy. This finding makes compound **4** the first salt-like mononuclear

ferric catecholate complex exhibiting valence tautomerism. It should be noted, that the possibility of the VT phenomenon in salt-like ferric catecholates was discussed earlier,[28,29,31] but was not observed. We assume, that the realization of the VT transition in [(TPA)Fe(3,6-DBCat)]BF_4 became possible due to the features of the used 3,6-di-*tert*-butyl-catecholate ligand. In contrast to the previously studied ferric complexes bearing substituted catecholates (H, alkyl, alkoxy, Cl, and NO_2), 3,6-DBCat is characterized by reduced redox-potential (close to 3,5-DBCat, but slightly lower)[62] and differs by steric properties.[63,64] This hypothesis is confirmed by the performed EPR investigations, which revealed the reduced anisotropy of the *g*-tensor in comparison with the literature.[31] All these features, most likely, favour the accessibility of the Fe^{II}-SQ state and, therefore, the possibility of VT transition.

Author contributions

Maxim Chegerev: Conceptualization, investigation, and writing – original draft. Oleg Demidov: Investigation. Pavel Vasilyev: Investigation. Nikolay Efimov: Investigation. Stanislav Kubrin: Investigation. Andrey Starikov: Conceptualization and investigation. Valery Vlasenko: Investigation. Alexander Piskunov: Investigation. Svetlana Shapovalova: Investigation and writing – original draft. Alexander Guda: Investigation and writing – original draft. Yury Rusalev: Investigation. Alexander Soldatov: Investigation and supervision.

Conflicts of interest

There are no conflicts to declare.

Acknowledgements

The work was financially supported by the Ministry of Science and Higher Education of the Russian Federation (State Assignment in the Field of Scientific Activity, No. 0852-2020-0019). Magnetochemical studies were performed using the equipment of the JRC PMR IGIC RAS.

References

1 C. G. Pierpont and R. M. Buchanan, *Coord. Chem. Rev.*, 1981, **38**, 45–87.
2 C. G. Pierpont, *Coord. Chem. Rev.*, 2001, **216–217**, 99–125.
3 A. I. Poddel'sky, V. K. Cherkasov and G. A. Abakumov, *Coord. Chem. Rev.*, 2009, **253**, 291–324.
4 W. Kaim and A. Paretzki, *Coord. Chem. Rev.*, 2017, **344**, 345–354.
5 K. I. Pashanova, A. I. Poddel'sky and A. V. Piskunov, *Coord. Chem. Rev.*, 2022, **459**, 214399.
6 I. L. Fedushkin, A. S. Nikipelov, A. G. Morozov, A. A. Skatova, A. V. Cherkasov and G. A. Abakumov, *Chem. – Eur. J.*, 2012, **18**, 255.
7 R. F. Munha, R. A. Zarkesh and A. F. Heyduk, *Dalton Trans.*, 2013, **42**, 3751.
8 J. Turek, H. Kampova, Z. Padelkova and A. Ruzicka, *J. Organomet. Chem.*, 2013, **25**, 745–746.
9 D. L. J. Broere, R. Plessius and J. I. van der Vlugt, *Chem. Soc. Rev.*, 2015, **44**, 6886–6915.
10 J. I. van der Vlugt, *Chem. – Eur. J.*, 2019, **25**, 2651–2662.
11 S. Demir, I.-R. Jeon, J. R. Long and T. D. Harris, *Coord. Chem. Rev.*, 2015, **289–290**, 149–176.
12 O. Drath and C. Boskovic, *Coord. Chem. Rev.*, 2018, **375**, 256–266.
13 I. V. Ershova, A. V. Piskunov and V. K. Cherkasov, *Russ. Chem. Rev.*, 2020, **89**, 1157.
14 M. G. Chegerev and A. A. Starikova, *Eur. J. Inorg. Chem.*, 2021, **2021**, 2684–2695.
15 O. Sato, *Nat. Chem.*, 2016, **8**, 644–656.
16 A. Dei and L. Sorace, *Appl. Magn. Reson.*, 2010, **38**, 139–153.
17 A. A. Starikova, M. G. Chegerev and A. G. Starikov, *Russ. J. Coord. Chem.*, 2020, **46**, 193–213.
18 H. G. Jang, D. D. Cox and L. Que Jr., *J. Am. Chem. Soc.*, 1991, **113**, 9200–9204.
19 P. Mialane, L. Tchertanov, F. Banse, J. Sainton and J.-J. Girerd, *Inorg. Chem.*, 2000, **39**, 2440–2444.
20 M. Pascaly, M. Duda, F. Schweppe, K. Zurlinden, F. K. Muller and B. Krebs, *J. Chem. Soc., Dalton Trans.*, 2001, 828–837.
21 M. Merkel, D. Schnieders, S. M. Baldeau and B. Krebs, *Eur. J. Inorg. Chem.*, 2004, 783–790.
22 Y. Hitomi, M. Yoshida, M. Higuchi, H. Minami, T. Tanaka and T. Funabiki, *J. Inorg. Biochem.*, 2005, **99**, 755–763.
23 M. Higuchi, Y. Hitomi, H. Minami, T. Tanaka and T. Funabiki, *Inorg. Chem.*, 2005, **44**, 8810–8821.
24 T. Funabiki, A. Fukui, Y. Hitomi, M. Higuchi, T. Yamamoto, T. Tanaka, F. Tani and Y. Naruta, *J. Inorg. Biochem.*, 2002, **91**, 151–158.
25 P. Gütlich and H. A. Goodwin, *Topics in Current Chemistry, Spin Crossover in Transition Metal Compounds I–III*, Springer Berlin Heidelberg, 2004.
26 *Spin-Crossover Materials: Properties and Applications*, ed. M. A. Halcrow, John Wiley & Sons, Chichester, 2013, p. 564.
27 A. J. Simaan, M.-L. Boillot, E. Rivire, A. Boussac and J.-J. Girerd, *Angew. Chem., Int. Ed.*, 2000, **39**, 196–198.
28 A. J. Simaan, M.-L. Boillot, R. Carrasco, J. Cano, J.-J. Girerd, T. A. Mattioli, J. Ensling, H. Spiering and P. Gütlich, *Chem. – Eur. J.*, 2005, **11**, 1779–1793.
29 S. Floquet, A. J. Simaan, E. Riviere, M. Nierlich, P. Thuery, J. Ensling, P. Gutlich, J.-J. Girerd and M.-L. Boillot, *Dalton Trans.*, 2005, 1734–1742.
30 D. J. Harding, P. Harding and W. Phonsri, *Coord. Chem. Rev.*, 2016, **313**, 38–61.
31 J.-J. Girerd, M.-L. Boillot, G. Blain and E. Rivière, *Inorg. Chim. Acta*, 2008, **361**, 4012–4016.

 This journal is © The Royal Society of Chemistry 2022

32 C. R. Tichnell, D. A. Shultz, C. V. Popescu, I. Sokirniy and P. D. Boyle, *Inorg. Chem.*, 2015, **54**, 4466–4474.
33 E. Evangelio and D. Ruiz-Molina, *Eur. J. Inorg. Chem.*, 2005, 2957–2971.
34 T. Tezgerevska, K. G. Alley and C. Boskovic, *Coord. Chem. Rev.*, 2014, **268**, 23–40.
35 Y. M. Chiou and L. Que Jr., *Inorg. Chem.*, 1995, **34**, 3577–3578.
36 D. H. Jo, Y. M. Chiou and L. Que Jr., *Inorg. Chem.*, 2001, **40**, 3181–3190.
37 W. O. Koch, V. Schünemann, M. Gerdan, A. X. Trautwein and H.-J. Krüger, *Chem. – Eur. J.*, 1998, **4**, 1255–1265.
38 T. R. Lakshman, S. Chatterjee, B. Chakraborty and T. K. Paine, *Dalton Trans.*, 2016, **45**, 8835–8844.
39 A. G. Starikov, M. G. Chegerev, A. A. Starikova and V. I. Minkin, *Russ. J. Coord. Chem.*, 2019, **45**, 675–679.
40 A. Beni, A. Dei, S. Laschi, M. Rizzitano and L. Sorace, *Chem. – Eur. J.*, 2008, **14**, 1804–1813.
41 I. N. Meshcheryakova, A. S. Shavyrin, A. V. Cherkasov and A. V. Piskunov, *Russ. Chem. Bull.*, 2019, **68**, 1414–1423.
42 *CrysAlisPro. Version 171.41.93a*, Rigaku Oxford Diffraction, 2015, **https://www.rigaku.com/products/crystallography/crysalis**.
43 G. M. Sheldrick, *Acta Crystallogr., Sect. A: Found. Adv.*, 2015, **71**, 3.
44 G. M. Sheldrick, *Acta Crystallogr., Sect. C: Struct. Chem.*, 2015, **71**, 340.
45 A. A. Chernyshov, A. A. Veligzhanin and Y. V. Zubavichus, *Nucl. Instrum. Methods Phys. Res., Sect. A*, 2009, **603**, 95–98.
46 M. J. Frisch, G. W. Trucks, H. B. Schlegel, G. E. Scuseria, M. A. Robb, J. R. Cheeseman, G. Scalmani, V. Barone, G. A. Petersson, H. Nakatsuji, X. Li, M. Caricato, A. V. Marenich, J. Bloino, B. G. Janesko, R. Gomperts, B. Mennucci, H. P. Hratchian, J. V. Ortiz, A. F. Izmaylov, J. L. Sonnenberg, D. Williams-Young, F. Ding, F. Lipparini, F. Egidi, J. Goings, B. Peng, A. Petrone, T. Henderson, D. Ranasinghe, V. G. Zakrzewski, J. Gao, N. Rega, G. Zheng, W. Liang, M. Hada, M. Ehara, K. Toyota, R. Fukuda, J. Hasegawa, M. Ishida, T. Nakajima, Y. Honda, O. Kitao, H. Nakai, T. Vreven, K. Throssell, J. A. Montgomery Jr., J. E. Peralta, F. Ogliaro, M. J. Bearpark, J. J. Heyd, E. N. Brothers, K. N. Kudin, V. N. Staroverov, T. A. Keith, R. Kobayashi, J. Normand, K. Raghavachari, A. P. Rendell, J. C. Burant, S. S. Iyengar, J. Tomasi, M. Cossi, J. M. Millam, M. Klene, C. Adamo, R. Cammi, J. W. Ochterski, R. L. Martin, K. Morokuma, O. Farkas, J. B. Foresman and D. J. Fox, *Gaussian 16, Revision C.01*, Gaussian, Inc., Wallingford, CT, 2016.
47 V. N. Staroverov, G. E. Scuseria, J. Tao and J. P. Perdew, *J. Chem. Phys.*, 2003, **119**, 12129.
48 A. V. Lado, A. I. Poddel'sky, A. V. Piskunov, G. K. Fukin, E. V. Baranov, V. N. Ikorskii, V. K. Cherkasov and G. A. Abakumov, *Inorg. Chim. Acta*, 2005, **358**, 4443–4450.
49 S. N. Brown, *Inorg. Chem.*, 2012, **51**, 1251–1260.
50 E. Munck, in *Physical Methods in Bioinorganic Chemistry*, ed. L. Que Jr., University Science Books, Sausalito, 2000, p. 287.
51 V. I. Goldanskii and S. V. Karyagin, *Phys. Status Solidi B*, 1975, **68**, 693–702.
52 V. García-López, J. C. Waerenborgh, B. J. C. Vieira, M. Clemente-León and E. Coronado, *Dalton Trans.*, 2018, **47**, 9156–9163.
53 P. Sadhukhan, S.-Q. Wu, J. I. Long, T. Nakanishi, S. Kanegawa, K. Gao, K. Yamamoto, H. Okajima, A. Sakamoto, M. L. Baker, T. Kroll, D. Sokaras, A. Okazawa, N. Kojima, Y. Shiota, K. Yoshizawa and O. Sato, *Nat. Commun.*, 2021, **12**, 4836.
54 A. Guda, M. Chegerev, A. Starikov, V. Vlasenko, A. Zolotukhin, M. Bubnov, V. Cherkasov, V. Shapovalov, Yu. Rusalev, A. Tereshchenko, A. Trigub, A. Chernyshev and A. Soldatov, *J. Phys.: Condens. Matter*, 2021, **33**, 215405.
55 W.-Q. Cheng, G.-L. Li, R. Zhang, Z.-H. Ni, W.-F. Wang and O. Sato, *J. Mol. Struct.*, 2015, **1087**, 68–72.
56 A. Bannwarth, S. O. Schmidt, G. Peters, F. D. Sonnichsen, W. Thimm, R. Herges and F. Tuczek, *Eur. J. Inorg. Chem.*, 2012, 2776–2783.
57 A. A. Starikova, M. G. Chegerev, A. G. Starikov and V. I. Minkin, *Comput. Theor. Chem.*, 2018, **1124**, 15–22.
58 J. Cirera, M. Via-Nadal and E. Ruiz, *Inorg. Chem.*, 2018, **57**, 14097–14105.
59 G. K. Gransbury, B. N. Livesay, J. T. Janetzki, M. A. Hay, R. W. Gable, M. P. Shores, A. Starikova and C. Boskovic, *J. Am. Chem. Soc.*, 2020, **142**, 10692–10704.
60 T. E. Westre, P. Kennepohl, J. G. DeWitt, B. Hedman, K. O. Hodgson and E. I. Solomon, *J. Am. Chem. Soc.*, 1997, **119**, 6297–6314.
61 A. Rakotonandrasana, D. Boinnard, J.-M. Savariault, J.-P. Tuchagues, V. Petrouleas, C. Cartier and M. Verdaguer, *Inorg. Chim. Acta*, 1991, **180**, 19–31.
62 G. A. Abakumov, M. P. Shurygina, S. A. Chesnokov, N. O. Druzhkov, M. A. Lopatin, Yu. V. Chechet and V. K. Cherkasov, *High Energy Chem.*, 2005, **39**, 299–303.
63 R. M. Buchanan, B. J. Fitzgerald and C. G. Pierpont, *Inorg. Chem.*, 1979, **18**, 3439–3444.
64 C. W. Lange, B. J. Conklin and C. G. Pierpont, *Inorg. Chem.*, 1994, **33**, 1276–1283.

This journal is © The Royal Society of Chemistry 2022